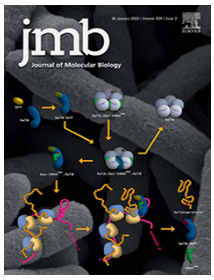

Structure of the Human TELO2-TTI1-TTI2 Complex

Youngran Kim [1,†], Junhyeon Park [1,†], So Young Joo [3], Byung-Gyu Kim [2], Aera Jo [1], Hyunsook Lee [3] and Yunje Cho [1,*]

*1 - **Department of Life Science,** Pohang University of Science and Technology, Pohang 37673, South Korea*
*2 - **Center for Genomic Integrity Institute for Basic Science (IBS),** UNIST, Ulsan 44919, South Korea*
*3 - **Department of Biological Sciences & Institute of Molecular Biology and Genetics,** Seoul National University, Seoul 08832, South Korea*

***Correspondence to Yunje Cho:** yunje@postech.ac.kr (Y. Cho)*
https://doi.org/10.1016/j.jmb.2021.167370
Edited by J. Buchner

Abstract

Phosphatidylinositol 3-kinase-related protein kinases (PIKKs) play critical roles in various metabolic pathways related to cell proliferation and survival. The TELO2-TTI1-TTI2 (TTT) complex has been proposed to recognize newly synthesized PIKKs and to deliver them to the R2TP complex (RUVBL1-RUVBL2-RPAP3-PIH1D1) and the heat shock protein 90 chaperone, thereby supporting their folding and assembly. Here, we determined the cryo-EM structure of the TTT complex at an average resolution of 4.2 Å. We describe the full-length structures of TTI1 and TELO2, and a partial structure of TTI2. All three proteins form elongated helical repeat structures. TTI1 provides a platform on which TELO2 and TTI2 bind to its central region and C-terminal end, respectively. The TELO2 C-terminal domain (CTD) is required for the interaction with TTI1 and recruitment of Ataxia-telangiectasia mutated (ATM). The N- and C-terminal segments of TTI1 recognize the FRAP-ATM-TRRAP (FAT) domain and the N-terminal HEAT repeats of ATM, respectively. The TELO2 CTD and TTI1 N- and C-terminal segments are required for cell survival in response to ionizing radiation.

Introduction

Phosphatidylinositol 3-kinase-related protein kinases (PIKKs) are members of the Ser/Thr kinase family that play pivotal roles in various pathways related to cell metabolism, proliferation, and differentiation.[1–5] Mammalian cells possess six PIKKs: Ataxia-telangiectasia mutated (ATM), Ataxia-telangiectasia and Rad3 related (ATR), DNA-dependent protein kinase catalytic subunit (DNA-PKcs), Mammalian target of rapamycin (mTOR), Suppressor of morphogenesis in genitalia (SMG-1), and Transformation/transcription domain-associated protein (TRRAP).[1–5] All except TRRAP possess kinase activities that promote a cascade of phosphorylation events in response to signals associated with DNA damage repair, cell size control, autophagy, cell cycle progression, and nonsense-mediated mRNA decay.[6–15] TRRAP is involved in transcription control.[16] These PIKKs share a similar domain arrangement, with Huntingtin, elongation factor 3, protein phosphatase 2A, and yeast kinase TOR1 (HEAT) repeats at the N-terminal end, and FRAP-ATM-TRRAP (FAT), kinase, and FATC domains at the C-terminal end.[1,2,4,5,17–23] Because of their significant roles, the stability of these PIKKs is crucial for cell metabolism and viability.

The TELO2-TTI1-TTI2 ternary complex (mammalian TTT complex; yeast Tel2-Tti1-Tti2) is

responsible for the assembly and stability of all PIKKs.[24–36] Each component of the complex is highly conserved in mammalian cells and their homologs, and homologs of low similarity are also present in yeast and *Caenorhabditis elegans (Ce)*. TTT is known to function as a co-chaperone together with heat shock protein 90 (HSP90) and R2TP (yeast Rvb1-Rvb2-Tah1-Pih1 or metazoan RUVBL1-RUVBL2- RPAP3-PIH1D1), and to specifically participate in the folding of newly synthesized PIKKs without affecting their mRNA levels.[25,26,29–36] Initially, Tel2 (Telomere length regulation protein 2; TELO2 in mammals, Clk-2 in *Ce*) was identified as a regulator of telomere length in yeast.[37–39] Subsequent studies revealed that Tel2/Clk-2 is involved in various cellular processes, such as cell proliferation, telomere maintenance, the biological clock, embryonic development, and the DNA damage checkpoint.[37–46] In more recent studies, knock-down of TELO2 resulted in a decrease in PIKKs at the protein level, suggesting that TELO2 directly regulates the stability of PIKKs.[24–34] Genome-wide screening of Tel2-binding proteins identified two associated proteins, Tel2-interacting protein 1 (Tti1) and Tel2-interacting protein 2 (Tti2).[27] Cells lacking Tti1 exhibited decreased levels of expression for all six PIKKs.[26–28] Knock-down of either TTI1 or TELO2 resulted in disassembly of mTORC1 and mTORC2.[28] Tti1 is responsible for resistance to DNA damage and controls the DNA damage checkpoint.[27] In the absence of Tti1, the expression level of Tel2 is diminished, implying that the two proteins function together. While TELO2 binds to part of the N-terminal HEAT repeats of ATM and mTOR,[25] TTI1 interacts with the N-terminal half containing the FAT domain of SMG-1.[30] Recent studies showed that Tti1-Tti2 interacts with the FAT and kinase domains of mTOR.[47] The importance of TTT assembly is illustrated by its association with syndromic intellectual disability and You-Hoover-Fong syndrome, which are caused by mutations of TTI1 and TELO2, respectively.[48,49]

The TTT complex functions together with R2TP and HSP90 chaperones.[25–31,33,34] R2TP is formed by the alternating assembly of two RUVBL1 and RUVBL2 ATPases into a heterohexameric ring. RPAP3 (Tah1 in yeast) and PIH1D1 (Pih1 in yeast) mediate indirect interaction between HSP90 and the TTT complex. In energy-rich conditions, the TTT complex interacts with the N-terminal PIH domain of PIH1D1 via the phosphorylated flexible loop of TELO2.[26,31,50–53] A recent study showed that the TTT complex can directly interact with RUVBL1 and RUVBL2 of the R2TP complex.[47]

At present, the molecular mechanism of TTT-mediated specific folding of PIKKs and assembly into larger complexes is poorly understood. Little is known about the structure and assembly of the TTT complex, how the three proteins of TTT stabilize each other, how the TTT adaptor recognizes PIKKs, and how the adapter delivers the substrate to HSP90 or R2TP. Furthermore, it is unclear if TTT stabilizes different PIKKs via different or similar binding and folding mechanisms. As an initial step toward understanding the mechanism by which TTT stabilizes PIKKs, we determined cryo-electron microscopy (EM) structures of TTT at an average resolution of 4.2 Å. We present full-length structures of TTI1 and TELO2 and a partial structure of TTI2. All three components adopt elongated helical repeat structures. TTI1 provides a platform on which TELO2 and TTI2 bind. TELO2 binds to the middle region of TTI1 via its N-terminal domain (NTD). The NTD of TTI2 binds to the C-terminal end of TTI1. Both TELO2 and TTI1 participate in the interaction with ATM. Yeast two-hybrid analysis revealed that the N- and C-segments of TTI1 bind to the C-terminal domain (CTD) and the N-terminal HEAT repeats of ATM, respectively. TELO2 CTD contributes to the stability of TTI1, and thereby head-to-tail ATM binding by TTI1. The TELO2 CTD and TTI1 N- and C-segments are required for cell survival following exposure to ionization radiation. The TTT complex structure provides insight into the mechanism by which TTI1 and TELO2 recognize the ATM kinase.

Results

Structure determination of the TELO2-TTI1-TTI2 complex

Size-exclusion chromatography and SDS-PAGE analyses showed that human TELO2, TTI1, and TTI2 form a stable complex with a molecular weight of ~400 kDa, a predicted hetero-trimer with a 1:1:1 molar ratio (Figure S1(a–c)). Single-particle cryo-EM analysis revealed three major classes of TELO2-TTI1-TTI2 complex structures comprised of helices. One of the major classes (32.3% of particles) corresponds to the TTT hetero-trimer (Figure 1(a–c), S1(d), S2(a–d); Table 1). The elongated EM density for a near-full-length TTI1 and the N-terminal TELO2 structures are well defined. Also, density for part of TTI2 is clearly observed, but the TELO2 CTD is visible only at lower contour levels.

In two of the five classes of the complex particles (class 1 and 4 in Figure S1(d)), density for TTI2 is clearly visible, whereas no density is observed for TTI2 in class 5 (right in Figure S1(d)), suggesting that TTI2 interacts with TTI1 in a flexible manner. To further analyze the structure of TTI2, we performed focused classification for TTI2 using over 1 million particles. We obtained five classes of TTI2 structures, among which an elongated density for TTI2 was observed in one class (~15%, class 5). By contrast, only weak density was observed in three classes, and another elongated but disconnected density from TTI1 was observed in class 4. A full-length TTI2 model predicted by AlphaFold fitted well into the map for

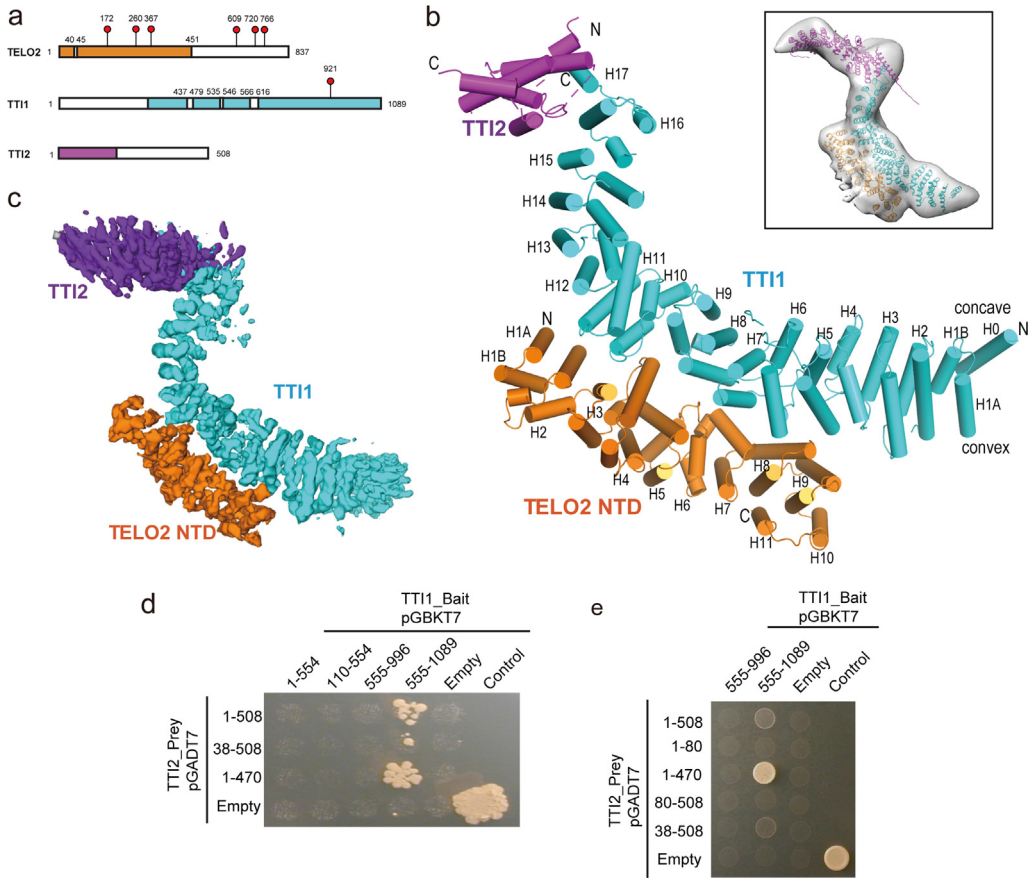

Figure 1. Cryo-EM structure of the human TTT complex. (a) Schematic diagram of the subdomains of human TELO2, TTI1, and TTI2, colored orange (TELO2 NTD), cyan (TTI1), and magenta (TTI2). Patient-derived mutations are indicated by red circles. Disordered regions are shown in white. (b) Cryo-EM map of the TTT complex at a global resolution of 4.2 Å. Each protein colored as in (a). (c) Overall structure of the TTT complex. The inset includes a model and a cryo-EM map (8.2 Å) from focused classification for human TTI2 (Figure S1d). The TTI2 model was derived from the Alphafold[68] model based on the human TTI2 sequence (UNIPROT ID: Q6NXR4). Each protein is colored as in (a). (d, e) Yeast two-hybrid analysis of the TTI1 and TTI2 deletion mutants. Selective plates (SD-LeuTrpAde) are shown. The master plate used to confirm growth of the mutants is shown in Figure S3a and S3b.

class 5 (Figure 1(b) inset, S1d). Thus, we concluded that TTI2 binds to TTI1 and undergoes dynamic movement in the TTT complex.

Despite limited resolution, we could assign the side chains of the following regions of TTI1 with the help of clusters of bulky hydrophobic side chains and the crystal structure of *Saccharomyces cerevisiae* (*Sc*) Tel2; residues 6–39 and 46–451 of TELO2, and the middle segment (helices H5A to H11B; residues 350–437, 479–535, 546–566, and 616–724) of TTI1 (Figure 1(a), S3; Table S1). Although we could not define the side chains, nine (H0 to H4B) and 11 (H12A to H17) helices are also visible at the N- and C-terminal ends of TTI1, respectively. Only six helices of TTI2 are visible near the end of TTI1.

The crystal structure of the *Sc*Tel2 NTD fitted well into the EM density of human TELO2. However, the orientations of TTI1 and TTI2 are ambiguous. To resolve this problem, we employed yeast two-hybrid analyses (Figure 1(d, e), S4(a, b)). We deleted the N-terminal half (residues 1–554) or the C-terminal half (residues 555–1089) of TTI1, and examined binding to full-length TTI2. While the TTI1 C-terminal fragment interacted with the full-length TTI2, the N-terminal fragment failed to interact with TTI2. Furthermore, the TTI1 fragments comprising residues 110–554 and 555–996 did not bind TTI2, suggesting that the C-terminal end (residues 997–1089) of TTI1 is important for interaction with TTI2 (Figure 1(d)). To identify the TTI1-interacting site within TTI2, we constructed four TTI2 fragments: residues 1–80, 1–470, 80–508, and 38–508. The TTI2 1–470 fragment interacts with the C-terminal region of TTI1 (Figure 1(d, e)). However, deletion of the N-terminal 37 residues of TTI2 abrogated the interaction between TTI1 and TTI2, suggesting that the N-terminal 37 residues of TTI2 are important for association between TTI1 and TTI2.

Table 1 Cryo-EM data collection, refinement and validation statistics.

	hTTT
Data collection and processing	
Magnification	79,000
Voltage (kV)	200
Total electron exposure (e-/Å^2)	42
Defocus range (μm)	−1.5 to −3.5 (Dataset I) −1.0 to −2.0 (Dataset II)
Pixel size (Å)	1.07
Symmetry imposed	C1
Initial particle images (no.)	2,553,890
Final particle images (no.)	323,679
Map resolution (Å)	4.2
FSC threshold	0.143
Refinement	
Model resolution (Å)	6.83
FSC threshold	0.5
Map sharpening B-factor (Å)	−206.6
Model composition	
Nonhydrogen atoms	8082
Protein residues	1227
B factors (Å)	
Protein	19.08
R.m.s. deviations	
Bond length (Å)	0.003
Bond angles (°)	0.746
Validation	
MolProbity score	2.35
Clashscore	17.15
Poor rotamers (%)	0
Ramachandran plot	
Favored (%)	87.07
Allowed (%)	12.68
Disallowed (%)	0.25

Interestingly, TTI2 fragments comprising residues 1–80 and 80–508 failed to interact with TTI1, suggesting that the two sites before and after residue 80 function cooperatively to associate with TTI1 (Figure 1(e)).

Overall structure of the TTT complex

All three proteins of the TTT complex are formed from helices, and mostly in the form of helical repeats, which eventually fold into α-solenoid structures (Figures 1(c) and 2(a, b)). TTI1 forms an elongated curve-shaped single domain (172 × 94 × 53 Å^3) comprised of 16 helical repeats with additional helical caps at the N- and C-terminal ends (Figure 2(b)). We divided the TTI1 solenoid into three segments based on the packing angle between the helical repeats: the N- (H0–Repeat 4), middle- (Repeat 5–9), and C-terminal (Repeat 10–H17) segments. The packing angles between most helical repeats are tilted in the range of 5–23°. However, the angles in repeats 4–5, 6–7, and 9–10 are 35.4°, 34.3°, and 39.1°, respectively (Figure 2(c)). These tilted repeats lead to the curved structure of TTI1. TELO2 is comprised of two domains with flat-shaped NTD and CTD regions connected by a highly flexible linker. The TELO2 NTD consists of nine helical repeats followed by two extended helices (Figure 2(a)).

The TTI1 middle region interacts with the TELO2 NTD, whereas the TTI1 C-terminal end binds to the TTI2 N-terminal segment. Overall, the TTT complex structure resembles a bird on the nest: TTI1 and TTI2 form the body and head of the bird, respectively, and TELO2 NTD forms the nest (Figure 1(b, c)). In the complex, the TTI1 and TELO2 NTDs are packed in an opposite direction: the inner surface of TTI1 is fully exposed, whereas the outer surface (Ha and Hc helices) faces toward the TELO2 NTD, so that the Ha helices of TTI1 and TELO2 NTD face each other (Figures 1(c) and 2(a, b)). The TELO2 CTD is closely positioned near the TTI1 middle segment. In the TTI1 and TTI2 interface, two or three helices of TTI2 participate in complex formation with the C-terminal H17 of TTI1.

TELO2 CTD is required for ATM binding

We observed EM density (density 1) for a cluster of helical repeats, into which we were able to fit the structure of the *Sc*Tel2 CTD near the interface between TTI1 (H5A and H6A) and the TELO2 NTD (PDB ID: 3O4Z; Figure 3(a–c)). Another region of density (density 2) was also observed close to density 1. However, we could not build structures into this second region of density because it could not be further resolved, but the overall dimension and shape of density 2 is close to the *Sc*Tel2 CTD. In the focused refinement, density 2 is only observed in one class, and most of density 2 is not present in the four other classes (Figure S1(d)). This suggests that the TELO2 CTD is highly flexible near the interface between TTI1 and the TELO2 NTD.

XL-MS analysis revealed that Lys200 of TTI1 is crosslinked to Lys678 of the TELO2 CTD, and Lys877 of TTI1 is crosslinked to Lys678 of the TELO2 CTD (Figure 3(d)). In the TTI1 structure, Lys200 and Lys877 are separated by 104 Å, far beyond the crosslinking distance from their TELO2 partner residues achievable by BS3. Because TELO2 NTD and CTD are connected by a ~80-residue flexible linker, TELO2 CTD is mobile with respect to TELO2 NTD. The NTDs of TELO2 and *Sc*Tel2 share structural similarity, with a root-mean-square deviation (rmsd) of 3.4 Å when all Cα atoms are aligned (Figure 3(a)). However, the flexible linker connecting the NTD and CTD is deleted in the structure of *Sc*Tel2 to aid crystallization.[29] When the NTDs are aligned, the *Sc*Tel2 CTD is distantly located from the *Sc*Tel2 NTD, whereas the CTD of human TELO2 is located much closer to the TELO2 NTD. Thus, although the TELO2 CTD does not stably interact with TTI1, the

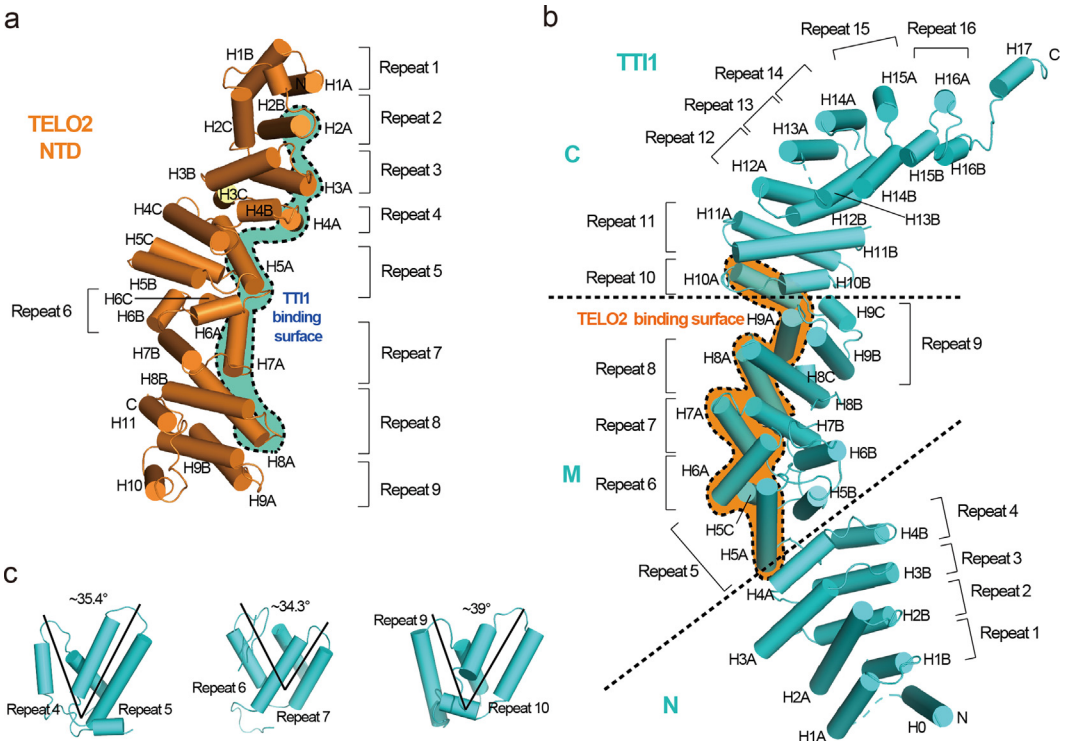

Figure 2. Close-up view of TELO2 and TTI1. (a) Close-up view of TELO2. The TTI1-interacting helices are highlighted with a dotted circle. (b) Close-up view of TTI1. The TELO2-interacting helices are highlighted with a dotted circle. (c) Enlarged view of the TTI1 helical repeats with a large inter-repeat packing angle. Left, Repeats 4 and 5; Middle, Repeats 6 and 7; Right, Repeats 9 and 10.

two components could come into proximity transiently.

Previous studies revealed that a TELO2 fragment containing residues 340–530 (both NTD and CTD) is involved in association with ataxia-telangiectasia and Rad3-related (ATR).[54,55] However, the role of TELO2 CTD in the co-chaperone function of PIKKs remains unclear. To investigate whether TELO2 CTD contributes to the binding of ATM, we made a CTD deletion mutant (residues 1–500; TELO2ΔC) and examined its interaction with ATM as well as TTI1 using pull-down assays (Figure 3(e), lanes 3 and 8). The TELO2ΔC mutant partly perturbed the interaction between TTI1 and TELO2, and the resulting complex exhibited reduced binding to ATM (Figure 3(e)). A simple explanation is that the TELO2 CTD directly interacts with ATM. Alternatively, it is also possible that because TTI1 and TELO2 depend on each other for their stability, removal of the TELO2 CTD might destabilize TTI1 or TELO2 NTD, and affect the interaction between TTI1 and TELO2, ultimately preventing interaction with ATM. Collectively, although the TELO2 CTD itself does not engage in a stable interaction with TTI1, it contributes to the formation of the TTI1-TELO2 complex and localization of ATM to the TTT complex.

Interaction between TELO2 and TTI1

In the three segments of TTI1, the middle region primarily interacts with TELO2. TTI1 binds to the center of the TELO2 NTD through its outer surface (Figure 4(a)). Both TTI1 and TELO2 form shallow pockets through which the two proteins interact in a complementary manner. The interface is extensive, burying 1282 Å^2 of surface area. For convenience, we divided the binding interface into three regions: interface 1 between the TTI1 middle segment (H9A and H10A) and TELO2 NTD (H2A, H3A, and H4A); interface 2 between the TTI1 middle part (H7A and H8A) and TELO2 NTD (H5C-H6A loop and H7A); and interface 3 between the N-terminal part (H5A and H6A) of the TTI1 middle segment, and the H8A helix and the following loop of the TELO2 NTD (Figure 4(a–c)). The buried surface area of interface 1 is 527 Å^2, while interfaces 2 and 3 bury 306 and 463 Å^2 of surface area, respectively. While hydrophobic interactions are dominant in interfaces 2 and 3, ionic and hydrogen bond (H-bond) interactions further stabilize these interfaces.

In interface 1, Tyr654 and Leu709 of TTI1 engage in hydrophobic interactions with Thr145, Pro147, and Leu151 of TELO2. His708 is within H-bond distance of Ser56 of TELO2 (Figure 4(b)).

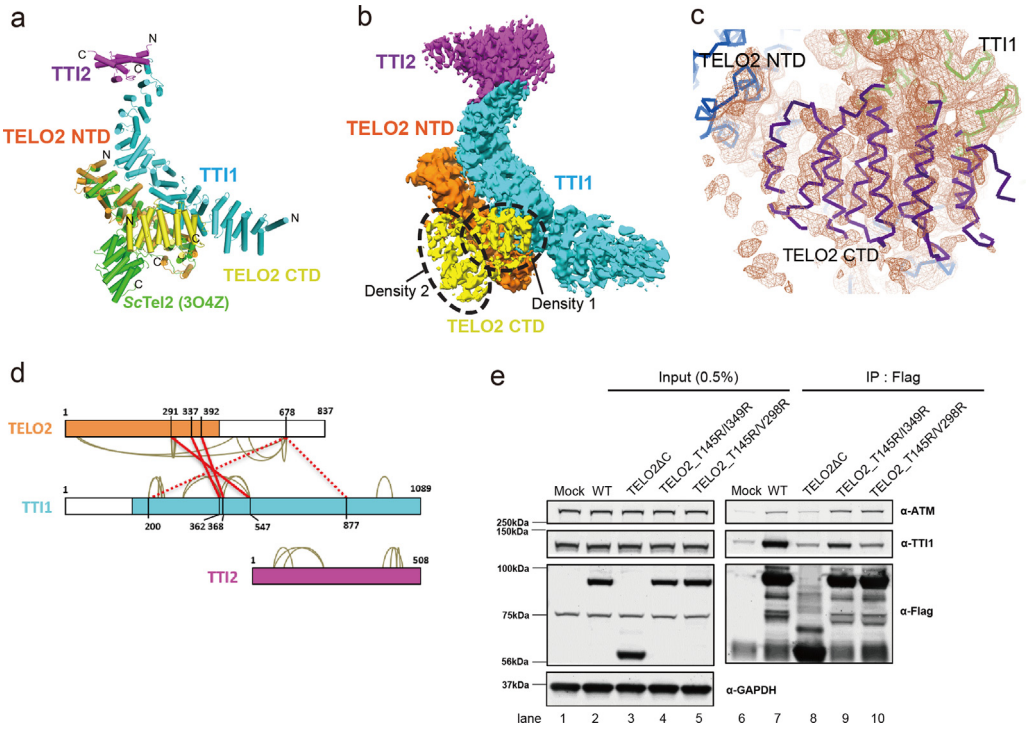

Figure 3. Structure of the TELO2 CTD. (a) Structure of the TTT complex. The TELO2 CTD is colored yellow. The structure of *Sc*Tel2 CTD (green, PDB ID: 3O4Z, residues 510–768) is superimposed on the NTD of TELO2. (b) Cryo-EM density for the TTT complex. Each protein is colored as in (a). (c) Enlarged view of the TELO2 CTD density (light red) with the *Sc*Tel2 CTD structure (purple). (d) XL-MS analysis of the TTT complex. Intra- and inter-molecular interactions are shown in thin red and solid gray lines, respectively. Intra-molecular interactions between the modeled regions are marked as red solid lines. Inter-molecular interactions between the modeled and non-modeled regions are marked as red dotted lines. Inter-molecular interactions are marked as solid gray lines. (e) Pull-down analysis of ATM and TTI1 by TELO2 mutants. Lanes 1–5 are lysates containing 0.5% of total proteins used for immunoprecipitation. Lanes 6–10 are eluted fractions. HEK293T cells were transfected with empty vector, Flag-tagged TTI1 wild-type, or Flag-tagged TTI1 mutants for 48 h. Flag-tagged TELO2 wild-type or Flag-tagged TELO2 mutants were isolated by Flag affinity purification using resin conjugated with anti-flag antibodies. Eluates were analyzed using the same gel employed for immunoblot exposure.

Interface 2 is formed by a mixture of hydrophobic interactions and H-bonds (Figure 4(c, d)). Tyr502 and Leu503 of TTI1 are packed against Val298 and Leu306 of TELO2. Glu563 of TTI1 forms an ion pair with Arg262 of TELO2. In interface 3, Ile373, Phe417, Val422, His424, and Leu425 of TTI1 are close to Ala348 and Ile349 of TELO2. Asn420 of TTI1 forms an H-bond with Thr342 of TELO2. Most of the residues described in the three interfaces are conserved in vertebrates (Figure 4(e), S5(a)).

XL-MS analysis revealed that Lys291 (H7A) of TELO2 is crosslinked to Lys547 (loop H7A-H7B) of TTI1, and their Cα-Cα distance is 19.8 Å (Figure 3(d)). Lys337 (H8A of TELO2) is crosslinked to Lys362 (loop H4B–H5A of TTI1), and Lys392 (H9A of TELO2) is linked to Lys368 (loop H4B–H5A), which are separated by 25 Å and 20 Å, respectively. This suggests that TELO2 and TTI1 interact in a head-to-tail manner, supporting our structure and yeast two-hybrid results.

To confirm the TELO2 residues involved in binding to TTI1 in our structure, we made two double mutants of TELO2, Thr145Arg/Ile349Arg (TI mutant) and Thr145Arg/Val298Arg (TV mutant), and examined their interaction (Figure 3(e)). Both double mutants exhibited significantly reduced binding to TTI1 relative to wild-type TELO2, confirming the importance of these residues of TELO2 in the association with TTI1. Previously, Leu395, Met407, and Leu425 of TELO2 were predicted to interact with TTI1-TTI2, and the corresponding mutation impaired several functions of yeast Tel2 associated with ATM, ATR, and mTOR.[29] In our structure, these residues are distant from the interface in the complex structure. However, exposed Leu395 and partly buried Met407 at the TELO2 NTD are relatively close to the TELO2 CTD (within 15–20 Å). Thus, it is possible that these residues are involved in interaction with PIKKs or with TELO2 CTD in a transient manner.

To investigate whether disruption of the TTI1-TELO2 interface affects the recruitment of ATM to the TTT complex, we performed pull-down analysis using TELO2 mutants. TELO2 TI and TV mutants exhibited slightly increased binding to ATM compared with wild-type TELO2, which suggests that disruption of the TTI1-TELO2 interface did not affect ATM recruitment by TELO2 or TTT complex (Figure 3(e)). However, we cannot exclude the possibility that the overexpression of TELO2 mutants compensated the weak association of TELO2 mutant with TTI1-TTI2 or ATM, and thereby recruit ATM.

To confirm the Tti1 residues at the interface in the structure, we also made three multiple mutants of TTI1 and disrupted the interaction between TTI1 and TELO2: Ser421Arg/Val422Arg in interface 2 and 3 (interface mutant 1, IM1); Gly701Arg/Leu709Arg in interface 1 (IM2); and Ser421Arg/Val422Arg/Gly701Arg/Leu709Arg in interface 1, 2,

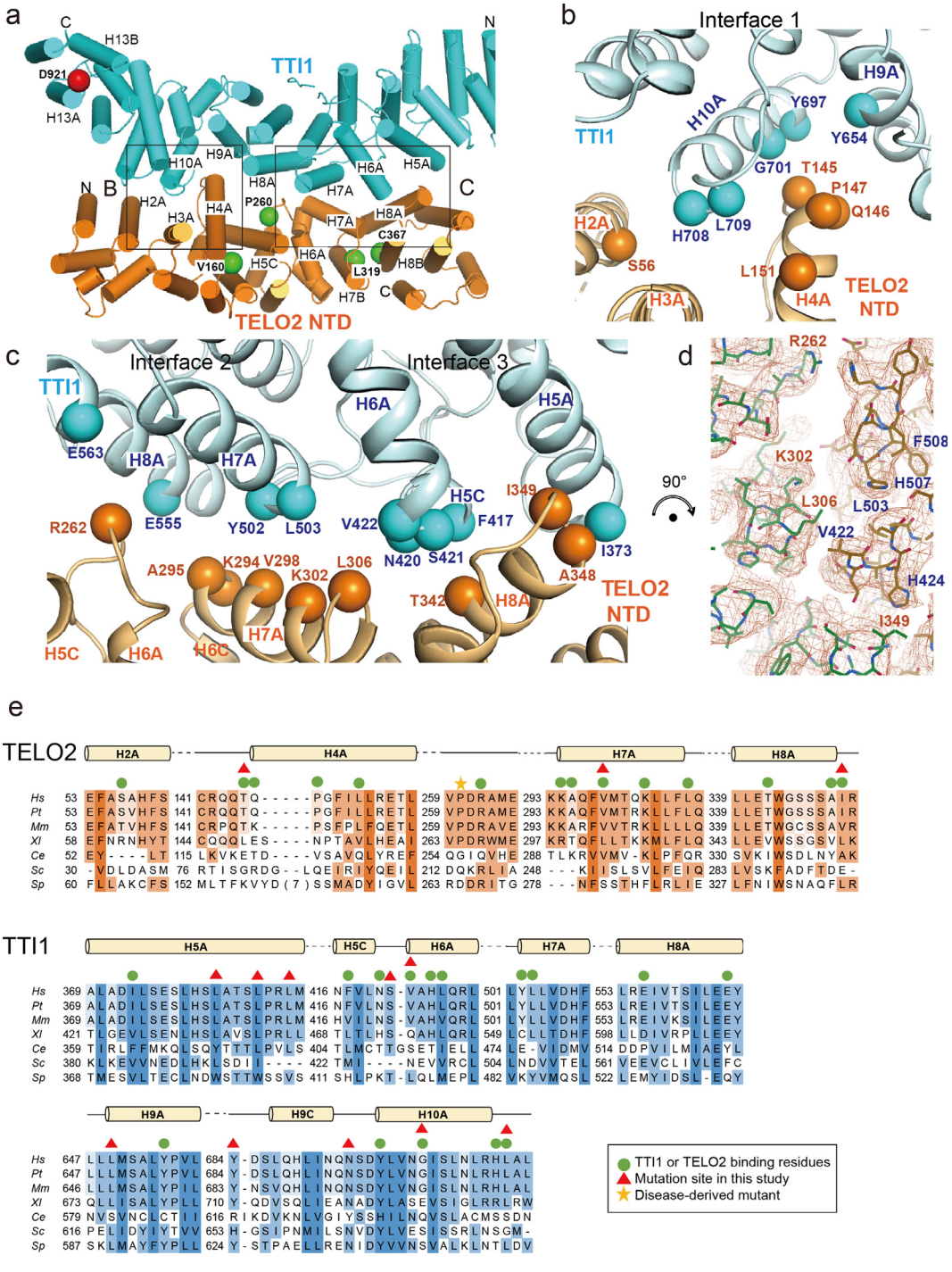

and 3 (IM3). We then examined binding of these TTI1 mutants to TELO2 (Figure 5(a)). Binding of the TTI1 IM1 and IM2 mutants to TELO2 was noticeably decreased compared with wild-type TTI1, and binding of the IM3 mutant was further decreased. This result validates the structure of the TTI1-TELO2 interface and supports the conclusion that TTI1 and TELO2 are dependent on each other for stability. All three TTI1 IM mutants exhibited binding of ATM similar to or slightly greater than that of wild-type TTI1, suggesting that disruption of the TTI1-TELO2 interface did not affect the binding of TTI1 to ATM. However, it is possible that endogenous TELO2 forms a sufficient quantity of TTT complex in cells expressing higher levels of exogenous TTI1 mutants, which allows the recruitment of ATM.

Head-to-tail binding of ATM to TTI1

Previously, TTI1 has been shown to interact with SMG-1.[30] To examine whether TTI1 interacts with other PIKKs and to identify the PIKK-binding site in TTI1, we performed yeast two-hybrid analysis; we generated several TTI1 and ATM constructs based on structural information, and examined interactions between the TTI1 and ATM fragments by yeast two-hybrid analysis (Figure 5(b)). The N-terminal segment of TTI1 (residues 1–365; H0 and repeats 1–4) interacted with the FAT domain of ATM (residues 1936–2680). The C-terminal segment of TTI1 (residues 779–1089; repeats 12–16 and H17) interacted with the N-terminal half (residues 1–533) of the HEAT repeat domain of ATM (Figure 5(b)). These results suggest that the N- and C-segments of TTI1 interact with ATM in a head-to-tail manner.

To confirm the yeast two-hybrid results, we performed pull-down analysis of TTI1, TELO2, and ATM. Due to the limited resolution of the TTI1 structure, we were only able to assign the side chains of residues at the middle region of TTI1, but not at the N- or C-segments that are critical for binding to ATM. Thus, we truncated the N- and C-terminal segments of TTI1 and examined interactions with endogenous ATM (Figure 5(a, c)). The N- (TTI1ΔN, 366–1089) and C-terminal truncated TTI1 constructs (TTI1ΔC, 1–996) were used to examine their interactions with ATM as well as TELO2. Consistent with yeast two-hybrid analysis, removal of the N- or C-terminal region weakened the interaction between TTI1 and ATM, demonstrating that TTI1 interacts with ATM via its N- and C-terminal segments. Because TTI2 is packed against the TTI1 C-terminal end, removal of the TTI1 C-terminal segment would abrogate TTI1-TTI2 complex formation, and decreased interaction with ATM could be partly due to liberation of TTI2 from TTI1. Removal of the N- or C-segment also affected the association of TTI1 with TELO2. The N-terminal segment of TTI1 does not make direct contact with TELO2. However, deletion of the N-terminal segment might affect the local structure of TTI1 (H4A and H5A), which form interface 3 between TTI1 and TELO2.

Next, we examined whether the middle region of TTI1 contributes to the binding to ATM; we performed a homology search for TTI1 and analyzed the protein-binding sites within homologous proteins. A DALI search revealed that the N-terminal segment of TTI1 is most similar to CLIP-Associating Protein 2 (CLASP2:3WOZ, Z score 8.5, rmsd for 192 Cα atoms 3.5 Å) and Protein Phosphatase 2A (PP2A: 3C5W, Z score 8.6, 192 Cα atoms 3.7 Å). The middle segment is most similar to Tuberous Sclerosis Complex 2 (TSC2:5HIU, Z score 9, rmsd for 290 Cα atoms 3.9 Å), and the C-terminal segment of TTI1 most resembles Importin α (6BVV: Z score 9.0, rmsd for 263 Cα atoms 3.8 Å; Figure 5(d), S6(a–f)). These proteins interact with their partners through

Figure 4. Interface between TELO2 and TTI1. (a) Dimeric interface between TELO2 (orange) and TTI1 (cyan). The boxes highlight the helices at the interface between TELO2 and TTI1. The mutations associated with You-Hoover-Fong syndrome, intellectual disability disorder patients, or model organisms are indicated by spheres. Each sphere is colored red (mutations on TTI1) or green (mutations on TELO2). (b, c) Clusters of residues involved in inter-molecular interactions divided into three patches: patch 1 (b) and patches 2 and 3 (c) shown in an orthogonal view to (a). (d) Cryo-EM density map of patches 2 and 3 shown looking down compared with the view in (c). (e) Structure-based sequence alignment of TELO2 and TTI1 using the PROMALS 3D program. Secondary structure assignment was based on the structures of TTI1 and TELO2. UniProt ID and NCBI GeneBank ID codes for sequences used for TELO2 are as follows: *Homo sapiens* (Q9Y4R8), *Pan troglodytes* (H2QAA3), *Mus musculus* (Q9DC40), *Xenopus laevis* (Q6GPP1), *Caenorhabditis elegans* (Q95YE9), *Saccharomyces cerevisiae* (P53038), and *Saccharomyces pombe* (Q9P3W5). UniProt ID and NCBI GeneBank ID codes for sequences used for TTI1 are as follows: *H. sapiens* (O43156), *P. troglodytes* (H2QKB8), *M. musculus* (Q91V83), *X. laevis* (XP_018096713.1), *C. elegans* (Q19378), *S. cerevisiae* (P36097), and *S. pombe* (O94600). Residues involved in TELO2-TTI1 interactions are illustrated as blue circles. Mutants used for pull-down assays and rescue experiments are indicated by red rectangles. The TELO2 and TTI1 mutants associated with You-Hoover-Fong syndrome and intellectual disability disorder patients are indicated by yellow stars. Invariant and highly conserved residues of TTI1 orthologs are highlighted in blue and sky blue, respectively, and those of TELO2 in orange or light orange, respectively.

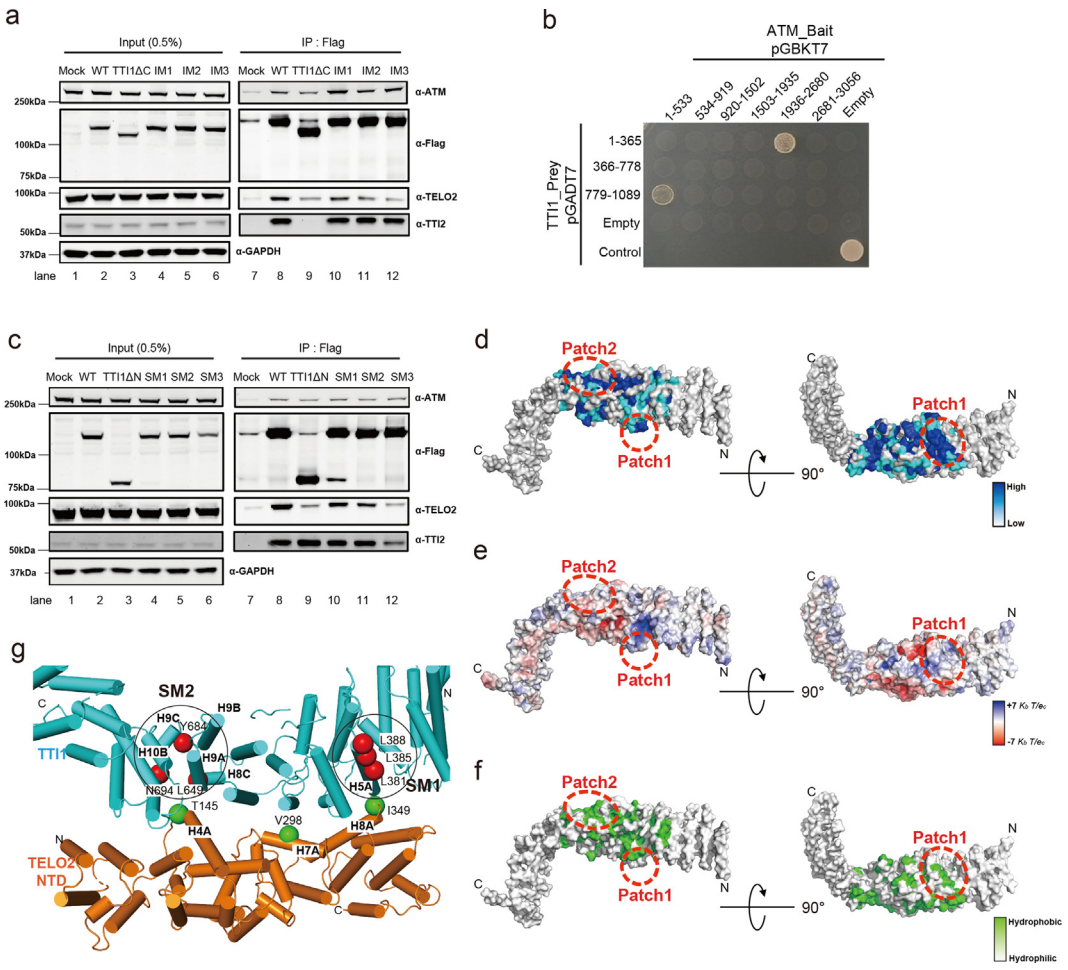

Figure 5. Binding of ATM to TTI1. (a, c) Immunoprecipitation analysis of ATM and TELO2 by TTI1 mutants. Lanes 1–6 are lysates containing 0.5% of total proteins used for immunoprecipitation. Lanes 7–12 are eluted fractions. HEK293T cells were transfected with empty vector, Flag-tagged TTI1 wild-type, or Flag-tagged TTI1 mutants for 48 h. Flag-tagged TTI1 wild-type or Flag-tagged TTI1 mutants were isolated by Flag affinity purification using resin conjugated with anti-flag antibodies. Eluates were analyzed using the same gel employed for immunoblot exposure. (b) Yeast two-hybrid analysis of interactions between TTI1 and ATM fragments. A selective plate for binding of TTI1 to ATM mutants (SD-LeuTrpHis3Ade) is shown. The master plate is shown in Figure S3c. (d) Surface representation of TTI1 with the degree of sequence conservation in two different views. Invariant residues among six species are colored blue, and less conserved residues (~80%) are colored cyan. Two different views of the TTI1 are shown. Left, the same view as in (g). Right, view rotated 90° along the x-axis in the left panel. The conserved surfaces were identified by mapping partner-interacting sites of structural homologs. (e) Electrostatic surface potential representations of TTI1. The electrostatic surface was calculated with APBS [69] and displayed using PyMOL. Positively and negatively charged regions are colored blue and red, respectively. Left and right panels are shown in the same orientation as in (d). (f) Surface representation of TTI1 showing hydrophobic residues colored green. Left and right panels are shown in the same orientation as in (d). (g) Structure showing the positions of the mutated residues. Residues at the surface of TTI1 are shown as red spheres.

specific binding regions corresponding to the following regions of TTI1: the concave region between repeats 10 and 14, the middle of the H5A and H6A helices, the H8C-H9A loop, the H9B-H9C loop, and the H9C-H10A loop. Using surface conservation and the protein-interacting region in the homologous proteins, we identified two clusters of conserved residues in the TTI1 middle region (Figure 5(d–f)): patch 1 at the H5A surface (Leu381, Leu385, and Leu388); and patch 2 between repeats 9 and 10 (Leu649, Tyr684, and Asn694). To investigate the importance of these regions in binding to PIKKs, we made three multiple mutants of the TTI1 surface: surface mutant 1 (SM1, Leu381Asn/Leu385Asn/Leu388Asn), surface mutant 2 (SM2, Leu649Ala/Tyr684Ala/Asn694Ala), and surface mutant 3 (SM3: Leu381Asn/Leu385Asn/Leu388Asn/Leu649Ala/Tyr684Ala/Asn694Ala; Figure 5(g)). While the TTI1 SM1 mutant associated with TELO2 to a similar

extent to wild-type TTI1, the SM2 and SM3 mutation exhibited slightly reduced binding to TELO2. This might be because the mutated residues of the SM1 mutant are fully exposed, whereas Leu649, Tyr684, and Asn694 in the SM2 mutant are located between helices H9 and H10, and hence partially buried, thereby affecting the local structure of TTI1. Despite the reduced binding to TELO2, all three SM mutants interacted with ATM with an affinity similar to that of wild-type TTI1 (Figure 5(c), lanes 10–12). Thus, similar to the IM mutants, the decreased binding of the TTI1 surface mutants to TELO2 did not affect their binding to ATM. Collectively, our results suggest that the N- and C-segments of TTI1, and the CTD of TELO2, contribute to ATM binding either via direct interaction or destabilization of the TTT complex.

Since deletion of the TELO2 CTD or the N- or C-segment of TTI1 affected the stability of ATM, we examined the sensitivity of cells expressing TELO2 or TTI1 mutants toward ionizing radiation (IR). We first confirmed that HeLa cells expressing siRNAs against TELO2 or TTI1 showed reduced levels of the corresponding protein (Figure 6(a, b)). Next, we expressed wild-type or mutant TELO2 or TTI1 in the siRNA-treated cells, and examined the survival of irradiated cells. Cells expressing TELO2ΔC showed decreased cell viability similar to that of TELO2-depleted cells at 3 Gy of IR (Figure 6(c)). This is consistent with the reduced ATM binding of TELO2ΔC. However, the

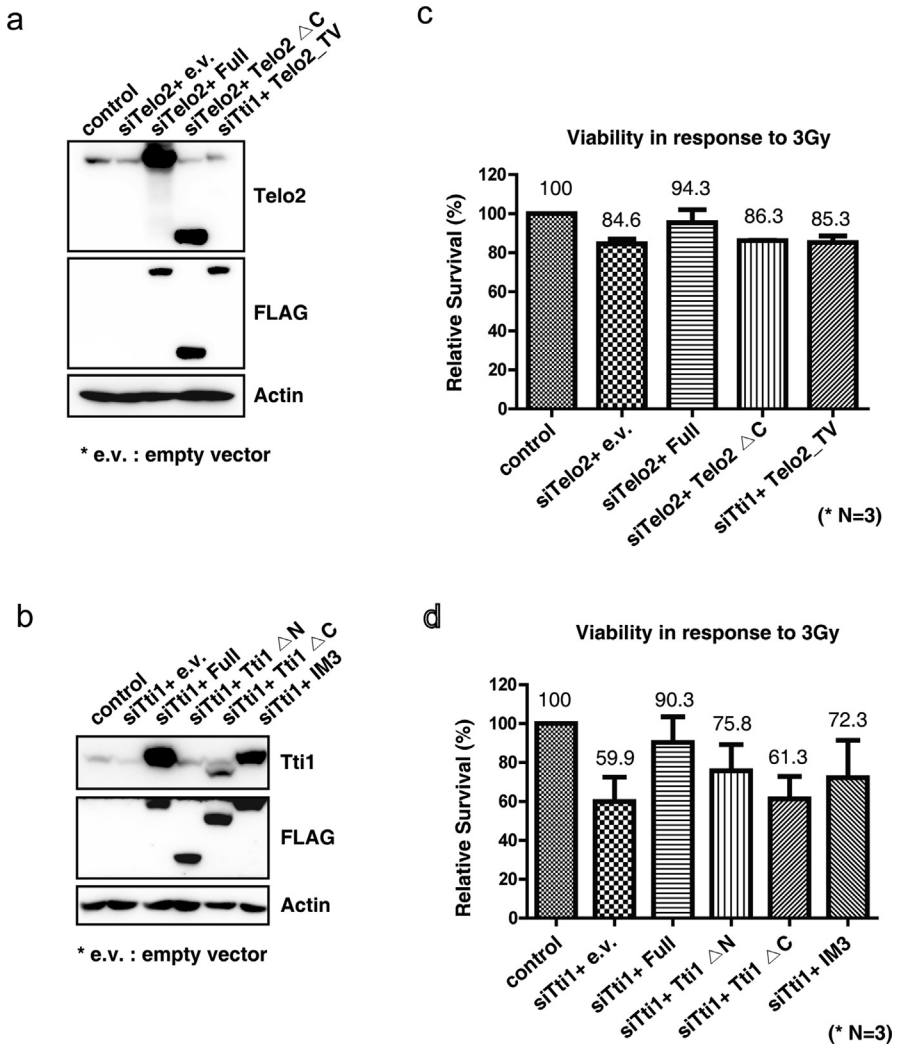

Figure 6. TELO2 and TTI1 are required for DNA damage resistance. (a) Western blotting analysis of cells in which TTI1 is depleted (lane 2) and cells expressing wild-type (lane 3) or mutant (lane 4–6) TTI1. (b) Western blotting analysis of cells in which TELO2 is depleted (lane 2) and cells expressing wild-type (lane 3) or mutant (lane 4–6) TELO2. (c) Viability of cells expressing wild-type or mutant TTI1 in response to 3 Gy of IR monitored by MTT assay. Error bars represent the standard deviation of three independent assays. (d) Viability of cells expressing wild-type or mutant TTI1 in response to 3 Gy of IR monitored by MTT assay. Error bars represent the standard deviation of three independent assays.

TELO2 TV mutant that retained ATM binding similar to wild-type TELO2 exhibited sensitivity to IR, which suggests that factors other than ATM might contribute to IR sensitivity.

TTI1-depleted cells were more sensitive to IR than TELO2-depleted cells, consistent with a previous report (Figure 6(d)).[27] Cells expressing TTI1ΔC with impaired ATM binding showed decreased viability similar to that of TELO2-depleted cells upon IR exposure, whereas cells expressing TTI1ΔN or TTI1 IM3 mutants showed decreased but weaker IR sensitivity than cells harboring TTI1ΔC. However, within the range of experimental error, cells expressing either of the two latter mutants exhibited clearly increased viability, presumably due to ATM binding to these mutant proteins.

Discussion

The TTT complex is a molecular adaptor that recognizes newly synthesized PIKKs and delivers them to the HSP90 chaperone via the R2TP complex, thereby assisting their folding and assembly.[26,32] Complex formation of TTI1, TTI2, and TELO2 is essential for the stability of each component, and the stability and assembly of PIKKs..[25–29,34,52] In this study, we determined the cryo-EM structure of the TTT complex, and revealed how the three TTT proteins stabilize each other, and how the complex recognizes ATM.

Molecular dynamics analysis suggests that α-solenoid proteins exhibit an end-to-end stretching behavior with reversible elasticity.[57] Hydrophobic interactions between HEAT repeats and conformational entropic effects are likely to contribute to the flexible behavior of the α-solenoid proteins, and to endow them with molten globule-like properties. In the TTT complex, extensive interaction between the middle TTI1 segment and the TELO2 NTD, and side-by-side packing between the TTI1 C-terminal end and TTI2, are expected to restrict the elasticity of the three TTT components and to protect them against cellular degradation. In our mutational analysis, removal of the TELO2 CTD or the TTI1 N-terminal segment might have failed to restrict the elasticity of their respective partners, resulting in decreased complex formation.

The TTT complex structure provides a possible explanation for disease-causing mutations of TTI1 and Tel2. It has been reported that Pro260Leu, Cys367Phe, Arg609His, Asp720Val, and Val766Met for TELO2, and Asp921Asn for TTI1, are associated with You-Hoover-Fong syndrome, and intellectual disability disorder patients;[48,49] mapping these mutations revealed that Pro260Leu (loop H5C-H6A) and Cys367Phe (H8B) can disrupt the environment of interfaces 2 and 3, respectively (Figure 4(a)). Thus, the structure predicts that the pathogenic effects of these mutations are due to destabilization of the local structure of TELO2, and consequently the TTT assembly. Asp921 is located in the H13A-H13B loop of TTI1, close to the interaction site between TTI1-TTI2. Therefore, this mutation might disrupt the TTI1 and TTI2 interaction or assembly of the TTT complex with R2TP.[48]

The Cys307Tyr mutant of *Schizosaccharomyces pombe (Sp)* Tel2 (Leu319 in human TELO2) is sensitive to DNA damage reagents, and the mutant strain failed to arrest at S phase.[56] The Cys307Tyr mutant strain exhibited decreased Rad3 (yeast ATR) protein levels and decreased affinity for Tti1 and Tti2, which suggests that an interface between Tti1 and Tel2 is important for controlling cell division by stabilizing ATR. Leu319 is positioned at H7B of TELO2, and mutation to a bulky residue might disrupt the hydrophobic interface between repeats 7 and 8, resulting in the destabilization of interfaces 2 and 3 (Figure 4(a)).

Both TELO2 and TTI1 recognize PIKK substrates. For example, TELO2 binds to the HEAT repeat (residues 830–1290), kinase, and FATC domains (2680–3056) of ATM, and the HEAT repeat domain of mTOR.[25] Both NTD and CTD (residues 350–530) of TELO2 are required for interaction with ATR.[54,55] However, the only available information for TTI1 is that the protein binds to the N-terminal half containing the HEAT repeats and FAT domain of SMG-1,[30] and TTI1-TTI2 interacts with the mTOR C-terminal region (residues 1376–2540) containing the FAT domain.[47] We further illuminated the TTI1 and PIKK interactions: TTI1 recognizes the N-terminal HEAT repeats (residues 779–1089) and FAT domain (1936–2680) of ATM through its CTD and NTD, respectively (Figure 7). The TELO2 CTD also plays a critical role in ATM binding either by stabilizing the TTT complex or directly interacting with ATM. The binding sites for TTI1 and TELO2 partly overlap at the N-terminal region of ATM but not at the C-terminal region of ATM. This suggests that TTI1 and TELO2 provide an extensive platform for the binding of ATM (Figure 7). It is possible that the two proteins have a complementary effect on ATM

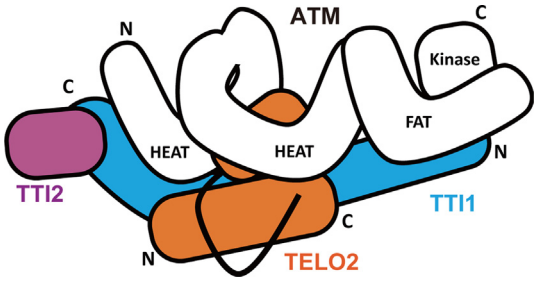

Figure 7. Model of the TTT and ATM complex. Interactions of TELO2 (orange), TTI1 (cyan), and TTI2 (magenta) with ATM are shown in cartoon representation.

binding. In an extended α-solenoid conformation, the N- and C-segments of TTI1 are separated by over 90 Å. Unfolded or partially folded PIKKs are predicted to expose various hydrophobic groups from the N-terminal HEAT repeats and C-terminal kinase domain, which could potentially form aggregates. By forming an extended interaction with the N- and C-terminal regions of ATM (or possibly other PIKKs) in an opposite direction, TTI1 or TTT complexes may prevent misfolding of ATM, which may explain why TTI1, the primary PIKK-binding protein in the TTT complex, adopts an extended helical conformation.

In our TTT complex structure, the TELO2 CTD is flexible but in a close proximity to the NTD and TTI1 interface. In the recently reported structure of TTT complexed with R2TP, the TELO2 CTD is invisible, presumably due to the flexibility of the linker connecting NTD and CTD, supporting the dynamic nature of the TELO2 CTD in the present study. By contrast, both NTD and CTD in *Sc*Tel2 are clearly defined and far more rigid, and there is no direct contact between the two domains. We reason that this is because CTD contacts the symmetry-related molecule in the crystal, and a flexible linker connecting the two domains was removed to aid crystallization.[29] Due to the extensive interface, we assumed that the TELO2 NTD should be sufficient to interact with TTI1. However, removal of the TELO2 CTD clearly affected TTI1 and ATM binding, as well as cell viability, suggesting that the TELO2 CTD might affect the stability of the TELO2 NTD and TTI1, which could be critical for ATM binding. Further analysis is required to understand the role of the TELO2 CTD.

Because TTI1 and TELO2 specifically recognize six unfolded or partially folded PIKKs sharing low sequence similarity, these proteins are likely to interact with PIKKs in a structure-specific manner. The TTI1-binding sites (HEAT repeats and FAT domains) in ATM are present in all PIKKs, despite differences in their overall structures.[17–23] Although we do not know the molecular details by which the HEAT repeats and FAT domains of PIKKs are recognized by TTI1 and TELO2, interactions between the HEAT repeats and the helical domain observed in the PIKK-partner complexes may provide clues: the HEAT repeats of mTOR bind to the ARM domain of regulatory-associated protein of mTOR (RAPTOR) and rapamycin-insensitive companion of mTOR (RICTOR)[17,22]; the N-terminal HEAT repeats of ATR recognize the HEAT repeat domain of ATRIP[19,23]; the HEAT repeats of DNA-PKCs bind to the helical bundle of the Ku80 C-terminal region.[18] We speculate that TTI1 and TELO2 bind the HEAT repeats and FAT domains in a manner similar to those between PIKK and partner complexes. Further studies are required to understand the molecular details of PIKK binding to TTT, and whether multiple substrates can be recognized by the TTT complex.

Materials and Methods

Cloning, expression, and purification of the human TTT complex

The cDNAs for human TTI1, TTI2, and TELO2 were generous gifts from Dr. KJ Myung (UNIST). DNAs encoding TTI1 and TTI2 were amplified by PCR and inserted into the pFastBac-Dual vector (*Eco*RI-*Not*I for TTI1 and *Nhe*I-*Xho*I for TTI2) with a non-cleavable 6 × His tag on the amino terminus of TTI1. The glutathione S-transferase (GST)-TELO2 fragment was inserted into the pFastBac-Dual vector (*Sal*I-*Not*I) with a human rhinovirus type 14 3C (HRV3C) protease-specific cleavage site. The Bac-to-Bac system (Invitrogen) was used to generate two types of baculoviruses in *Spodoptera frugiperda* (sf9) cells harboring TELO2 and TTI1-TTI2. To purify the TTT complex, 0.8–1.6 l sf9 cells were co-infected with two baculoviruses at a multiplicity of infection (MOI) of 13.3 and harvested at 84 h after infection. The infected cells were resuspended in His-affinity A buffer (25 mM Tris–HCl pH 7.5, 300 mM NaCl, 5 mM β-mercaptoethanol, 5% glycerol) and sonicated. The resulting supernatant was loaded onto a HiTrap His HP column (GE Healthcare), and eluted using His-affinity B buffer (25 mM Tris–HCl pH 7.5, 300 mM NaCl, 5 mM β-mercaptoethanol, 0.5 M imidazole, 5% glycerol) via an imidazole gradient. After HRV3C protease treatment during dialysis, we employed cation exchange chromatography using buffer comprising 25 mM Tris–HCl pH 7.5, 5 mM dithiothreitol (DTT), and 5% glycerol with a 0–600 mM NaCl gradient to remove the protease. Peak fractions containing the TTT complex were collected, concentrated, and stored at −80 °C.

Cryo-EM sample preparation and image acquisition

Prior to single-particle cryo-EM analysis, we prepared fresh TTT complex using size-exclusion chromatography with a Superose 6 10/300 GL column (GE Healthcare) in buffer comprising 20 mM HEPES pH 8.0, 200 mM NaCl, 2 mM DTT, and 1% glycerol. The highest peak fractions were collected, and 0.003% n-dodecyl-β-D-maltopyranoside (DDM) was added. A 3 μl volume of TTT complex (0.8–0.9 mg/ml) was loaded onto negatively discharged carbon grids (c-flat Co 1.2/1.3 400 mesh grid, EMS) with a PELCO EasiGlow (Ted Pella) by applying a current of 15 mA for 90 s. The grids were plunge-frozen in liquid ethane using a Vitrobot Mark IV (FEI) operating at 4 °C with 100% humidity and blotted for 6–8 s with a blot force 2 setting. Images were acquired using a Talos Arctica transmission electron microscope (FEI) operated at 200 kV equipped with a Gatan K3 summit direct electron detector (Photon Science Center, POSTECH) at

nominal magnification 79,000× with a pixel size of 1.07 Å per pixel at the specimen level.

Two datasets were collected comprising 7048 (Dataset I) and 13,755 (Dataset II) movies. Movies were collected at a dose rate of ~14 electrons per Å^2 per s with a defocus ranging from −1.5 to −3.5 μm (Dataset I) or −1.0 to −2.0 μm (Dataset II). The total exposure time was 3 s, and intermediate frames were recorded in 0.07 s intervals, resulting in an accumulated dose of 42 electrons per Å^2 and a total of 50 frames per micrograph.

Data processing

Movie frames were aligned and dose-weighted using MotionCor2,[58,59] and motion-corrected sums were used to estimate the contrast transfer function (CTF) using CTFFIND4.[60] In all, 147 micrographs were selected, and particles were picked using a template from pre-processed results using cryoSPARC v.2.14.[61] Automatically picked particles were subjected to one round of unsupervised 2D classification for 50 classes, and 6,190 particles of nine classes were selected to generate a model using Topaz within the cryoSPARC platform.[62] A total of 2,553,890 particles were picked from 20,803 micrographs using Topaz Extract based on the model generated by Topaz train and extracted with a box size of 350 pixels. Contaminants and false-positive particles were removed by several rounds of 2D classification. The selected particle projections were further subjected to 3D classification using *ab initio* reconstruction and heterogeneous refinement in cryoSPARC. A total of 1,002,216 particles were retained for further processing, and subjected to *ab initio* reconstruction and 3D heterogeneous refinement into five classes with C1 symmetry. Although three of the five classes embodied the structure of the TTT complex, one class revealed a clear heat repeat architecture and good connectivity of TTI1 and TELO2 NTD in the TTT complex. This class included 323,679 particles and was further improved by performing non-uniform refinement, resulting in a map with a global resolution of 4.2 Å according to a Fourier shell correlation (FSC) criterion of 0.143. The final map was sharpened using local sharpening algorithms in DeepEMhancer.[63]

Focused classification

To analyze the conformation of TTI2 and the TELO2 CTD in the TTT complex, focused classification was performed on 1,002,216 particles corresponding to the TTT complex generated by cryoSPARC:[62] for TTI2, we generated a mask around the TTI1 and TELO2 main body using MaskCreation in RELION-3.0.8.[58] Subtraction of a signal around the mask yielded particles with TTI2 and parts of the TTI1 C-terminal region. Subtracted particles were subjected to 3D-focused classification without a mask, avoiding biased classification. Five classes of 3D maps were computed, each of which showed a unique conformation for TTI2.

For the TELO2 CTD, we generated a mask around the TTT complex main body using MaskCreation in RELION-3.0.8.[58] Subtraction of a signal around the mask yielded particles with only a TELO2 CTD signal. Subtracted particles were subjected to 3D-focused classification without a mask, avoiding biased classification. Five classes of 3D maps were computed, each of which showed a unique conformation for TELO2 CTD. For the final map reconstruction, we performed a round of 3D auto-refinement with reverted particles from each class.

Model building

Model building was performed using COOT.[64] Initially, a number of helices were placed into the cryo-EM map, and a region corresponding to the TELO2 NTD was identified. We placed the structure of *Sc*Tel2 NTD (PDB ID: 3O4Z) into the map and further improved the model by manual building. Density for bulky residues including Tyr, Phe, and Trp guided us to assign and confirm the side chains of the TELO2 model. The side chains on the core part of the TTT complex are relatively well defined in the density map, and clusters of bulky hydrophobic side chains guided the tracing of residues 6–40 and 45–451 of TELO2. Only part of TTI2 is visible at the TTI1 end in the local resolution 7–10 Å EM density map, into which we were able to model six helices.

Most of the TTI1 main-chains were built *de novo* and connected using a poly-Ala model (~166–1071) comprising residues 166–222, 233–437, 475–535, 538–570, 616–774, and 857–1071. However, we could only assign the TTI1 side chains at the TELO2-binding interface, which contains residues 350–437, 479–535, 546–566, and 616–724. The TTT model was refined against the EM map using real space refine in PHENIX v.1.15.[65] The refined model had a MolProbity[66] score of 2.35 and a Clashscore of 17.15. All models and maps were visualized and rendered in UCSF Chimera[67] and PyMOL (v.2.0; Schrödinger, LLC).

Crosslinking mass spectrometry (XL-MS) analysis

For crosslinking mass spectrometry experiments, freshly prepared bissulfosuccinimidyl suberate (BS3, Thermo Fischer Scientific) dissolved in buffer for crosslinking (20 mM HEPES pH 8.0, 150 mM NaCl, 1 mM DTT, 5% glycerol) was added to the TTT complex at a final concentration of 2.5 mM, and the complex was crosslinked for 30 min on ice. Crosslinking was quenched by addition of 1.5 M Tris–HCl (pH 8.0) to a final concentration of 30 mM and incubation for 15 min on ice. Crosslinked TTT complex was separated

by SDS-PAGE. For liquid chromatography-tandem mass spectrometry (LC-MS/MS) analyses, the gel was de-stained, and bands were cut and processed. Briefly, TTT complex proteins bands were divided into 10 mm sections and subjected to in-gel digestion with trypsin. The tryptic digests were separated by online reversed-phase chromatography using an Eazy nano LC 1200 UHPLC (Thermo Fischer Scientific) equipped with an autosampler using a reversed-phase peptide trap Acclaim PepMap 100 column (75 μm inner diameter, 2 cm length) and a reversed-phase analytical PepMap RSLC C18 column (75 μm inner diameter, 15 cm length, 3 μm particle size), both from Thermo Fischer Scientific, followed by electrospray ionization at a flow rate of 300 nl/min. Samples were eluted using a split gradient of 3–50% solution B comprising 80% acetonitrile (can) with 0.1% formic acid (FA) over 60 min and 50–80% solution B over 10 min, followed by column washing with 100% solution B for 10 min. The chromatography system was coupled in line with an Orbitrap Fusion Lumos mass spectrometer.

The mass spectrometer was operated in XL-MS non-cleavable MS2-assisted high-energy collision-induced dissociation (HCD) mode with a 60,000 resolution MS1 scan (375–1500 m/z), in AGC target or max injection time auto-adjust mode. Peptides above a threshold of 5.0e4 and 3–8 charges were selected for fragmentation with dynamic exclusion for 30 s with a 10 ppm tolerance. Activation mode for MS2 scans was HCD (assisted collision energy 25% or 30%) at a resolution of 30,000. To identify chemically crosslinked peptides, spectra were searched against an in-house TTI complex database using Proteome Discoverer 2.4 with the Xlinkx algorithm (v.2.0), with peptide tolerance 10 ppm, fragment tolerance 0.02 Da, trypsin as protease with maximum four missed cleavage sites, carbamidomethylation on cysteine, oxidation of methionine and Tris-quenched BS3 (mass shift + 259.142 Da) as variable modifications, and a 1% false discovery rate (FDR).

Yeast two-hybrid assay

Yeast two-hybrid assays were performed by Panbionet (http://panbionet.com). The cDNAs for human full-length ATM were generous gifts from DS Lim (KAIST). The genes encoding human TTI1, TTI2, and ATM were amplified by PCR and cloned into both pGBKT7 and pGADT7 vectors (Clontech). The resulting plasmids were transformed into the AH109 yeast strain, which expresses HIS3 and ADE2 reporters. Each of the transformants was separately cultured on plates containing SD-LeuTrp, SD-LeuTrpAde2, and SD-LeuTrpHis3Ade2 medium. Interaction between bait and prey proteins reconstituted the function of GAL4 and activated reporter gene expression. Positive control yeast cells were transformed with pGBKT7-p53 bait plasmid and pGADT7-SV40 Tag prey plasmid. Negative control cells were transformed with parental bait vector (pGBKT7) and prey vector (pACT2).

Cell culture and antibodies

HEK293T cells were grown in Dulbecco's modified Eagle's medium (DMEM, Lonza) supplemented with 10% fetal bovine serum (FBS, Welgene or VWR Life Science) and 1× anti-anti (Gibco). During transfection, HEK293T cells were grown in DMEM supplemented with 10% FBS. Antibodies used for western blot analysis were anti-TELO2 rabbit polyclonal antibody (#15975-1-AP, Proteintech), anti-TTI1 mouse polyclonal antibody (#sc-271638, Santa Cruz Biotechnology), and anti-ATM rabbit polyclonal antibody (#2873, Cell Signaling Technology). Antibodies were diluted in 5% skim milk (Bio-Rad) containing TBST and 0.064–0.1% w/v NaN_3.

Pull-down assay

The genes encoding human TELO2 and TTI1 were cloned into the pCDNA3.1(+) Zeo vector (Invitrogen) using *Nhe*I and *Not*I. The full-length TELO2 and TTI1 constructs were fused with a Flag tag at the N-terminal end. Mutations were introduced in the same way described above. Transfections for transient expression of TELO2, TTI1, and mutant constructs were performed using Lipofectamine 2000 transfection reagent (Invitrogen) according to the manufacturer's protocol.

Transfected HEK293T cells were incubated for 48 h and then washed twice with phosphate-buffered saline (PBS, pH 7.4, Welgene). The cells were resuspended in binding buffer (25 mM Tris–HCl pH 8.0, 150 mM NaCl, 1 mM DTT, 1 mM EDTA, 0.3% w/v CHAPS hydrate, 10% glycerol), containing 0.1 mM phenylmethylsulfonyl fluoride (PMSF) and protease inhibitor cocktail (Roche). Lysates were homogenized and centrifuged at high speed in a microcentrifuge. Supernatants were collected, and protein concentration was quantified by Protein assay dye reagent (Bio-Rad). For pull-down assays, 2–3 mg total protein was incubated with 40 μl Anti-DYKDDDDK G1 Affinity Resin (GenScript) for 2 h. The resin was washed five times with binding buffer, and proteins were eluted with one column volume of binding buffer supplemented with 0.4 mg/ml Flag peptide.

Western blot analysis

Cell lysates and eluted proteins were prepared as described above. For immunoprecipitation analysis, cell lysates and eluted proteins were mixed with 5× Laemmli sample buffer. Samples were subsequently separated by SDS-PAGE and

transferred to nitrocellulose membranes (Millipore). The membranes were incubated in 5% skim milk (Bio-Rad) in TBST buffer (25 mM Tris–HCl, 140 mM NaCl, 0.1% Tween-20). Primary and secondary antibodies were incubated in TBST supplemented with 5% skim milk. Blotting bands were detected using a LI-COR Odyssey infrared imaging system.

Cell viability assay

HEK293FT cells were co-transfected with siRNA and DNA constructs of interest using Lipofectamine 2000 transfection reagent (Invitrogen) according to the manufacturer's protocol. Cells were treated with 0 or 3 Gy of γ-irradiation at 24 h post-transfection. Next, 3×10^3 cells per well were seeded in 96-well plates and cultured for 3 days, and the viability of cells was evaluated by MTT assay. Cells were incubated with 0.5 mg/ml MTT (Sigma-Aldrich) dissolved in DMSO added to the culture medium for 3 h at 37 °C. The amount of dye formed was quantified at a wavelength of 570 nm. The survival rates of irradiated cells were normalized to that of untreated cells for graphical representation. Three independent assays were performed.

Data availability

Atomic coordinates and the cryo-EM map have been deposited in the PDB and the EM Data Bank under accession numbers of 7F4U and EMD-31454, respectively.

CRediT authorship contribution statement

Youngran Kim: Conceptualization, Validation, Writing. **Junhyeon Park:** Conceptualization, Validation. **So Young Joo:** Conceptualization, Validation. **Byung-Gyu Kim:** Validation. **Hyunsook Lee:** Supervision. **Yunje Cho:** Conceptualization, Validation, Writing - review & editing, Supervision.

Acknowledgments

We thank to Ok-kyu Song, Nao Yoon and Jung Soon Koh for technical supports. This work was supported by grants from the National Research Foundation of Korea (NRF) funded by the Korea government (MEST, No. 2021R1A2C301335711, 2018R1A2A1A19021035, 2017M3A9F6029733 and 2017M3A9F6029736), BK21 program (Ministry of Education) to Y.C. The authors declare that none of the authors have a financial interest related to this work.

Author contributions

Y.K. carried out protein expression, purification and structure determination; Y.K. and J.H.P. performed biochemical experiments with the help of A.J., S.J. and H.L.; B.K. carried out mass spectrometry analysis; Y.K. and Y.C. designed research and wrote the manuscript.

Declaration of interests

The authors declare that they have no known competing financial interests or personal relationships that could have appeared to influence the work reported in this paper.

Appendix A. Supplementary material

Supplementary data to this article can be found online at https://doi.org/10.1016/j.jmb.2021.167370.

Received 28 June 2021;
Accepted 15 November 2021;
Available online 24 November 2021

Keywords:
PIKKs;
TELO2-TTI1-TTI2 complex;
protein folding;
protein stability;
cryo-EM

† These authors contributed equally to this work.

Abbreviations:
ATM, ataxia-telangiectasia mutated; cryo-EM, cryo-electron microscopy; FAT, FRAP-ATM-TRRAP; HEAT, Huntingtin, elongation factor 3, protein phosphatase 2A, and yeast kinase TOR1; HSP90, heat shock protein 90; PIKKs, phosphatidylinositol 3-kinase-related protein kinases; R2TP, RUVBL1-RUVBL2-RPAP3-PIH1D1; TTT, TELO2-TTI1-TTI2; XL-MS, crosslinking mass spectrometry

References

1. Shiloh, Y., (2003). ATM and related protein kinases: safeguarding genome integrity. *Nat. Rev. Cancer.* **3**, 155–168.
2. Abraham, R.T., (2004). PI3-kinase related kinases: 'big' players in stress-induced signaling pathways. *DNA Repair (Amst.)* **3**, 883–887.
3. Bakkenist, C.J., Kastan, M.B., (2004). Initiating cellular stress responses. *Cell* **118**, 9–17.
4. Lempiäinen, H., Halazonetis, T.D., (2009). Emerging common themes in regulation of PIKKs and PI3Ks. *EMBO J.* **28**, 3067–3073.
5. Baretić, D., Williams, R.L., (2014). PIKKs–the solenoid nest where partners and kinases meet. *Curr. Opin. Struct. Biol.* **29**, 134–142.

6. Cortez, D., Qin, G.J., Elledge, S.J., (2001). ATR and ATRIP: partners in checkpoint signaling. *Science* **294**, 1713–1716.
7. Shiloh, Y., (2006). The ATM-mediated DNA-damage response: taking shape. *Trends Biochem. Sci.* **31**, 402–410.
8. Guertin, D.A., Sabatini, D.M., (2007). Defining the role of mTOR in cancer. *Cancer Cell.* **12**, 9–22.
9. Harper, J.W., Elledge, S.J., (2007). The DNA damage response: ten years after. *Mol. Cell.* **28**, 739–745.
10. Kanu, N., Behrens, A., (2007). ATMIN defines an NBS1-independent pathway of ATM signalling. *EMBO J.* **26**, 2933–2941.
11. Branzei, D., Foiani, M., (2008). Regulation of DNA repair throughout the cell cycle. *Nat. Rev. Mol. Cell. Biol.* **9**, 297–308.
12. Cimprich, K.A., Cortez, D., (2008). ATR: An Essential Regulator of Genome Integrity. *Nat. Rev. Mol. Cell. Biol.* **9**, 616–627.
13. Maréchal, A., Zou, L., (2013). DNA damage sensing by the ATM and ATR kinases. *Cold Spring Harb. Perspect. Biol.* **5**, a012716
14. Kurosaki, T., Maquat, L.E., (2016). Nonsense-mediated mRNA decay in humans at a glance. *J. Cell. Sci.* **129**, 461–467.
15. Blackford, A.N., Jackson, S.P., (2017). ATM, ATR, and DNA-PK: The Trinity at the Heart of the DNA Damage Response. *Mol. Cell* **66**, 801–817.
16. Murr, R., Vaissière, T., Sawan, C., Shukla, V., Herceg, Z., (2007). Orchestration of chromatin-based processes: mind the TRRAP. *Oncogene* **26**, 5358–5372.
17. Yang, H., Jiang, X., Li, B., Yang, H.J., Miller, M., Yang, A., et al., (2017). Mechanisms of mTORC1 activation by RHEB and inhibition by PRAS40. *Nature* **552**, 368–373.
18. Sharif, H., Li, Y., Dong, Y., Dong, L., Wang, W.L., Mao, Y., et al., (2017). Cryo-EM structure of the DNA-PK holoenzyme. *Proc. Natl. Acad. Sci. U.S.A.* **114**, 7367–7372.
19. Rao, Q., Liu, M., Tian, Y., Wu, Z., Hao, Y., Song, L., et al., (2018). Cryo-EM structure of human ATR-ATRIP complex. *Cell. Res.* **28**, 143–156.
20. Xiao, J., Liu, M., Qi, Y., Chaban, Y., Gao, C., Pan, B., et al., (2019). Structural insights into the activation of ATM kinase. *Cell. Res.* **29**, 683–685.
21. Langer, L.M., Gat, Y., Bonneau, F., Conti, E., (2020). Structure of substrate-bound SMG1-8-9 kinase complex reveals molecular basis for phosphorylation specificity. *Elife* **9**, e57127
22. Scaiola, A., Mangia, F., Imseng, S., Boehringer, D., Berneiser, K., Shimobayashi, M., et al., (2020). The 3.2-Å resolution structure of human mTORC2. *Sci. Adv.* **6**, eabc1251.
23. Williams, R.M., Yates, L.A., Zhang, X., (2020). Structures and regulations of ATM and ATR, master kinases in genome integrity. *Curr. Opin. Struct. Biol.* **61**, 98–105.
24. Collis, S.J., Barber, L.J., Clark, A.J., Martin, J.S., Ward, J. D., Boulton, S.J., (2007). HCLK2 is essential for the mammalian S-phase checkpoint and impacts on Chk1 stability. *Nat. Cell. Biol.* **9**, 391–401.
25. Takai, H., Wang, R.C., Takai, K.K., Yang, H., de Lange, T., (2007). Tel2 regulates the stability of PI3K-related protein kinases. *Cell* **131**, 1248–1259.
26. Horejsí, Z., Takai, T., Adelman, C.A., Collis, S.J., Flynn, H., Maslen, S., et al., (2010). CK2 phospho-dependent binding of R2TP complex to TEL2 is essential for mTOR and SMG1 stability. *Mol. Cell* **39**, 839–850.
27. Hurov, K.E., Cotta-Ramusino, C., Elledge, S.J., (2010). A genetic screen identifies the Triple T complex required for DNA damage signaling and ATM and ATR stability. *Genes Dev.* **24**, 1939–1950.
28. Kaizuka, T., Hara, T., Oshiro, N., Kikkawa, U., Yonezawa, K., Takehana, K., et al., (2010). Tti1 and Tel2 are critical factors in mammalian target of rapamycin complex assembly. *J. Biol. Chem.* **285**, 20109–20116.
29. Takai, H., Xie, Y., de Lange, T., Pavletich, N.P., (2010). Tel2 structure and function in the Hsp90-dependent maturation of mTOR and ATR complexes. *Genes Dev.* **24**, 2019–2030.
30. Izumi, N., Yamashita, A., Iwamatsu, A., Kurata, R., Nakamura, H., Saari, B., et al., (2010). AAA+ proteins RUVBL1 and RUVBL2 coordinate PIKK activity and function in nonsense-mediated mRNA decay. *Sci. Signal* **3**, ra27.
31. Izumi, N., Yamashita, A., Hirano, H., Ohno, S., (2012). Heat shock protein 90 regulates phosphatidylinositol 3-kinase-related protein kinase family proteins together with the RUVBL1/2 and Tel2-containing co-factor complex. *Cancer Sci.* **103**, 50–57.
32. Kim, S.G., Hoffman, G.R., Poulogiannis, G., Buel, G.R., Jang, Y.J., Lee, K.W., et al., (2013). Metabolic stress controls mTORC1 lysosomal localization and dimerization by regulating the TTT-RUVBL1/2 complex. *Mol. Cell* **49**, 172–185.
33. Inoue, H., Sugimoto, S., Takeshita, Y., Takeuchi, M., Hatanaka, M., Nagao, K., et al., (2017). CK2 phospho-independent assembly of the Tel2-associated stress-signaling complexes in Schizosaccharomyces pombe. *Genes Cells* **22**, 59–70.
34. Sugimoto, K., (2018). Branching the Tel2 pathway for exact fit on phosphatidylinositol 3-kinase-related kinases. *Curr. Genet.* **64**, 965–970.
35. Shin, S.H., Lee, J.S., Zhang, J.M., Choi, S., Boskovic, Z.V., Zhao, R., et al., (2020). Synthetic lethality by targeting the RUVBL1/2-TTT complex in mTORC1-hyperactive cancer cells. *Sci. Adv.* **6**, eaay9131.
36. Guo, Y., Tocchini, C., Ciosk, R., (2021). CLK-2/TEL2 is a conserved component of the nonsense-mediated mRNA decay pathway. *PLoS One* **16**, e0244505
37. Lustig, A.J., Petes, T.D., (1986). Identification of yeast mutants with altered telomere structure. *Proc. Natl. Acad. Sci. U.S.A.* **83**, 1398–1402.
38. Runge, K.W., Zakian, A.K., (1996). TEL2, an essential gene required for telomere length regulation and telomere position effect in Saccharomyces cerevisiae. *Mol. Cell. Biol.* **16**, 3094–3105.
39. Kota, R.S., Runge, K.W., (1998). The yeast telomere length regulator TEL2 encodes a protein that binds to telomeric DNA. *Nucleic Acids Res.* **26**, 1528–1535.
40. Hartman, P.S., Herman, R.K., (1982). Radiation-sensitive mutants of Caenorhabditis elegans. *Genetics* **102**, 159–178.
41. Lakowski, B., Hekimi, S., (1996). Determination of life-span in Caenorhabditis elegans by four clock genes. *Science* **272**, 1010–1013.
42. Ahmed, S., Alpi, A., Hengartner, M.O., Gartner, A., (2001). C. elegans RAD-5/CLK-2 defines a new DNA damage checkpoint protein. *Curr. Biol.* **11**, 1934–1944.

43. Bénard, C., McCright, B., Zhang, Y., Felkai, S., Lakowski, B., Hekimi, S., (2001). The C. elegans maternal-effect gene clk-2 is essential for embryonic development, encodes a protein homologous to yeast Tel2p and affects telomere length. *Development* **128**, 4045–4055.
44. Lim, C.S., Mian, I.S., Dernburg, A.F., Campisi, J., (2001). C. elegans clk-2, a gene that limits life span, encodes a telomere length regulator similar to yeast telomere binding protein Tel2p. *Curr. Biol.* **11**, 1706–1710.
45. Jiang, N., Bénard, C.Y., Kébir, H., Shoubridge, E.A., Hekimi, S., (2003). Human CLK2 links cell cycle progression, apoptosis, and telomere length regulation. *J. Biol. Chem.* **278**, 21678–21684.
46. Shikata, M., Ishikawa, F., Kanoh, J., (2007). Tel2 is required for activation of the Mrc1-mediated replication checkpoint. *J. Biol. Chem.* **282**, 5346–5355.
47. Pal, M., Muñoz-Hernandez, H., Bjorklund, D., Zhou, L., Degliesposti, G., Skehel, J.M., et al., (2021). Structure of the TELO2-TTI1-TTI2 complex and its function in TOR recruitment to the R2TP chaperone. *Cell. Rep.* **36**, 109317
48. Karaca, E., Harel, T., Pehlivan, D., Jhangiani, S.N., Gambin, T., Akdemir, Z.C., et al., (2015). Genes that affect brain structure and function identified by rare variant analyses of Mendelian neurologic disease. *Neuron* **88**, 499–513.
49. You, J., Sobreira, N.L., Gable, D.L., Jurgens, J., Grange, D.K., Belnap, N., et al., (2016). A Syndromic Intellectual Disability Disorder Caused by Variants in TELO2, a Gene Encoding a Component of the TTT Complex. *Am. J. Hum. Genet.* **98**, 909–918.
50. Fernández-Sáiz, V., Targosz, B., Lemeer, S., Eichner, R., Langer, C., Bullinger, L., et al., (2013). SCFFbxo9 and CK2 direct the cellular response to growth factor withdrawal via Tel2/Tti1 degradation and promote survival in multiple myeloma. *Nat. Cell. Biol.* **15**, 72–81.
51. Pal, M., Morgan, M., Phelps, S.E.L., Roe, S.M., Parry-Morris, S., Downs, J.A., et al., (2014). Structural basis for phosphorylation-dependent recruitment of Tel2 to Hsp90 by Pih1. *Structure* **22**, 805–818.
52. Hořejší, Z., Stach, L., Flower, T.G., Joshi, D., Flynn, H., Skehel, J.M., et al., (2014). Phosphorylation-dependent PIH1D1 interactions define substrate specificity of the R2TP cochaperone complex. *Cell. Rep.* **7**, 19–26.
53. Henri, J., Chagot, M.E., Bourguet, M., Abel, Y., Terral, G., Maurizy, C., et al., (2018). Deep Structural Analysis of RPAP3 and PIH1D1, Two Components of the HSP90 Co-chaperone R2TP Complex. *Structure* **26**, 1196–1209.
54. Danielsen, J.M.R., Larsen, D.H., Schou, K.B., Freire, R., Falck, J., Bartek, J., et al., (2009). HCLK2 is required for activity of the DNA damage response kinase ATR. *J. Biol. Chem.* **284**, 4140–4147.
55. Xie, L., Pi, X., Mishra, A., Fong, G., Peng, J., Patterson, C., (2012). PHD3-dependent hydroxylation of HCLK2 promotes the DNA damage response. *J. Clin. Invest.* **122**, 2827–2836.
56. Xu, Y.J., Khan, S., Didier, A.C., Wozniak, M., Liu, Y., Singh, A., et al., (2019). A tel2 Mutation That Destabilizes the Tel2-TTI1-TTI2 Complex Eliminates Rad3 ATR Kinase Signaling in the DNA Replication Checkpoint and Leads to Telomere Shortening in Fission Yeast. *Mol. Cell. Biol.* **39**, e00175–e219.
57. Kappel, C., Zachariae, U., Dölker, N., Grubmüller, H., (2010). An Unusual Hydrophobic Core Confers Extreme Flexibility to HEAT Repeat Proteins. *Biophys J.* **99**, 1596–1603.
58. Zivanov, J., Nakane, T., Forsberg, B.O., Kimanius, D., Hagen, W.J.H., Lindahl, E., et al., (2018). New tools for automated high-resolution cryo-EM structure determination in RELION-3. *Elife* **7**, e42166
59. Zheng, S.Q., Palovcak, E., Armache, J.P., Verba, K.A., Cheng, Y.F., Agard, D.A., (2017). MotionCor2: anisotropic correction of beam-induced motion for improved cryo-electron microscopy. *Nat. Methods* **14**, 331–332.
60. Rohou, A., Grigorieff, N., (2015). CTFFIND4: Fast and accurate defocus estimation from electron micrographs. *J. Struct. Biol.* **192**, 216–221.
61. Punjani, A., Rubinstein, J.L., Fleet, D.J., Brubaker, M.A., (2017). cryoSPARC: algorithms for rapid unsupervised cryo-EM structure determination. *Nat. Methods* **14**, 290–296.
62. Bepler, T., Morin, A., Rapp, M., Brasch, J., Shapiro, L., Noble, A.J., et al., (2019). Positive-unlabeled convolutional neural networks for particle picking in cryo-electron micrographs. *Nature Methods* **16**, 1153–1160.
63. Sanchez-Garcia, R., Gomez-Blanco, J., Cuervo, A., et al., (2021). DeepEMhancer: a deep learning solution for cryo-EM volume post-processing. *Commun. Biol.* **4**, 874.
64. Emsley, P., Cowtan, K., (2004). Coot: model-building tools for molecular graphics. *Acta Crystallogr. D* **60**, 2126–2132.
65. Afonine, P.V., Poon, B.K., Read, R.J., Sobolev, O.V., Terwilliger, T.C., Urzhumtsev, A., et al., (2018). Real-space refinement in PHENIX for cryo-EM and crystallography. *Acta Crystallogr. D* **74**, 531–544.
66. Prisant, M.G., Williams, C.J., Chen, V.B., Richardson, J.S., Richardson, D.C., (2020). New tools in molprobity validation: CaBLAM for CryoEM Backbone, UnDowser to rethink 'Waters', and NGL viewer to recapture online 3D graphics. *Protein Sci.* **29**, 315–329.
67. Pettersen, E.F., Goddard, T.D., Huang, C.C., Couch, G.S., Greenblatt, D.M., Meng, E.C., et al., (2004). UCSF Chimera–a visualization system for exploratory research and analysis. *J. Comput. Chem.* **25**, 1605–1612.
68. Jumper, J., Evans, R., Pritzel, R., Green, T., Figurnov, M., Ronneberger, O., et al., (2021). Highly accurate protein structure prediction with AlphaFold. *Nature* **596**, 583–589.
69. Baker, N.A., Sept, D., Joseph, S., Holst, M.J., McCammon, J.A., (2001). Electrostatics of nanosystems: application to microtubules and the ribosome. *Proc. Natl. Acad. Sci. U.S. A.* **98**, 10037–10041.